Applied Energy 393 (2025) 126054

Contents lists available at ScienceDirect

Applied Energy

journal homepage: www.elsevier.com/locate/apen

Liquid hydrogen storage, thermal management, and transfer-control system for integrated zero emission aviation (IZEA)

Parmit S. Virdi [a,b], Wei Guo [a,b,*], Louis N. Cattafesta III [c], Peter Cheetham [d,e], Lance Cooley [a,b,f], Jonathan C. Gladin [g,h], Jiangbiao He [i], Chul Kim [e], Hui Li [d,e], Juan Ordonez [a,e], Sastry Pamidi [d,e], Jian-Ping Zheng [j]

[a] *Mechanical Engineering Department, FAMU-FSU College of Engineering, 2525 Pottsdamer St, Tallahassee, 32310, FL, USA*
[b] *National High Magnetic Field Laboratory, 1800 E Paul Dirac, Tallahassee, 32310, FL, USA*
[c] *Illinois Institute of Technology, 10 West 32th Street, Chicago, 60616, IL, USA*
[d] *Electrical and Computer Engineering Department, FAMU-FSU College of Engineering, 2525 Pottsdamer St, Tallahassee, 32310, FL, USA*
[e] *Center for Advance Power Systems, 2000 Levy Avenue, Tallahassee, 32310, FL, USA*
[f] *Applied Superconductivity Center, 2031 E Paul Dirac Dr, Tallahassee, 32310, FL, USA*
[g] *Daniel Guggenheim School of Aerospace Engineering, Georgia Tech, North Avenue, Atlanta, 30332, GA, USA*
[h] *Aerospace Systems Design Laboratory, 275 Ferst Drive NW, Atlanta, 30332, GA, USA*
[i] *Department of Electrical Engineering and Computer Science, University of Tennessee, 1520 Middle Dr, Knoxville, 37996, Tennessee, USA*
[j] *Department of Electrical Engineering, University at Buffalo, 230 Davis Hall University at Buffalo, North Campus, Buffalo, 14260, NY, USA*

HIGHLIGHTS

- Designed an integrated system combining liquid hydrogen storage, thermal management, and transfer control for hybrid-electric aircraft.
- Optimized a system-level fuel gravimetric index to 0.62, ensuring efficient hydrogen storage and utilization in aviation.
- Leveraged liquid hydrogen's dual functionality as both a fuel source and a cooling agent for power systems.
- Developed counterflow heat exchangers for effective thermal management of superconducting and other power components.
- Regulated tank pressure to maintain consistent hydrogen flow and cooling during varying flight conditions.
- Demonstrated significant potential for reducing carbon emissions and contrails in aviation.
- Provided a scalable solution for adopting hydrogen as a sustainable aviation fuel.

ARTICLE INFO

Keywords:
Zero emission aviation
Liquid hydrogen
Thermal management
Flow control

ABSTRACT

The rapid growth of the aviation sector underscores the urgent need to reduce carbon and contrail emissions, key contributors to climate change. Hydrogen, with its high specific chemical energy, emerges as a promising clean fuel alternative. To promote sustainable aviation, we propose an innovative design for a liquid hydrogen storage, thermal management, and transfer-control system tailored for Integrated Zero Emission Aviation (IZEA). Our design harnesses the cooling power of liquid hydrogen to manage the temperature and thermal loads on essential power system components. By regulating the pressure in the storage tank, we demonstrate the feasibility of delivering the required hydrogen mass flow rates—up to 0.25 kg/s—to meet a peak power demand of 16.2 MW for a prototype 100-passenger hybrid-electric aircraft, while efficiently cooling the power system using practical heat exchangers. Through comprehensive system-level optimization, we have identified the optimal tank and heat exchanger configurations that maximize the overall gravimetric index to a value of 0.62, where the index is defined as the ratio of the hydrogen fuel mass to the total mass of the fuel, storage tank, and thermal management system. Our findings emphasize the critical importance of system-level optimization in determining key design parameters, paving the way for zero-emission aviation technologies and advancing environmental sustainability in the aviation industry.

* Corresponding author at: Mechanical Engineering Department, FAMU-FSU College of Engineering, 2525 Pottsdamer St, Tallahassee, 32310, FL, USA
Email address: wguo@magnet.fsu.edu (W. Guo).

https://doi.org/10.1016/j.apenergy.2025.126054
Received 22 January 2025; Received in revised form 17 April 2025; Accepted 3 May 2025
Available online 8 May 2025

Nomenclature

Fuel properties

ρ_{LH_2}	Density of saturated liquid hydrogen at 20 K (kg/m^3)
ρ_{GH_2}	Density of saturated vapor hydrogen at 20 K (kg/m^3)
μ_{LH_2}	Dynamic viscosity of saturated liquid hydrogen at 20 K (Pa · s)
μ_{GH_2}	Dynamic viscosity of saturated vapor hydrogen at 20 K (Pa · s)
H_{fg}	Hydrogen specific enthalpy for vaporization (kJ/kg)
H_{LH_2}	Specific enthalpy of saturated liquid hydrogen at 20 K (kJ/kg)
H_{GH_2}	Specific enthalpy of saturated vapor hydrogen at 20 K (kJ/kg)
$\mathcal{E}_{LH_2}$	Specific internal energy of saturated liquid hydrogen at 20 K (kJ/kg)
$\mathcal{E}_{GH_2}$	Specific internal energy of saturated vapor hydrogen at 20 K (kJ/kg)

Fuel and working fluids parameters

$T^i_{H_2,in}$, $T^i_{H_2,ex}$	Inlet and exit temperatures of fuel in the ith heat exchanger (K)
$T^i_{wf,in}$, $T^i_{wf,ex}$	Inlet and exit temperatures of working fluid (K)
$H^i_{H_2,in}$, $H^i_{H_2,ex}$	Inlet and exit enthalpies of fuel (kJ/kg)
$H^i_{wf,in}$, $H^i_{wf,ex}$	Inlet and exit enthalpies of working fluid (kJ/kg)
C^i_{p,H_2}	Fuel specific heat (J/kg · K)
$C^i_{p,wf}$	Working fluid specific heat (J/kg · K)
k^i_{wf}	Working fluid thermal conductivity (W/m · K)
$k^i_{H_2}$	Fuel thermal conductivity (W/m · K)

Heat transfer parameters

h	Heat transfer coefficient (W/m^2 · K)
k_{ins}	Thermal conductivity of tank insulation (W/m · K)
$\dot{Q}_{leak}$	Rate of heat leakage to the tank (kW)
T_s	Insulation outer surface temperature (K)
E_i	Fuel total internal energy after refilling (kJ)
E_f	Fuel internal energy at P_{vent} (kJ)
ϕ_l^2	Two-phase friction multiplier

Tank parameters

P_{tank}	Pressure in hydrogen storage tank (bar)
V_{LH_2}	Initial liquid hydrogen volume in the tank (m^3)
m_{LH_2}	Initial liquid hydrogen mass in the tank (kg)
m_{wall}	Mass of the hydrogen tank wall (kg)
m_{ins}	Mass of the hydrogen tank insulation (kg)
V	Volume of hydrogen storage tank (m^3)
δ_w	Thickness of the hydrogen tank wall (mm)
δ_{ins}	Tank insulation thickness (cm)
ρ_w	Wall material density (kg/m^3)
A	Tank surface area (m^2)
y	Volume fraction of LH_2

Heat exchanger parameters

L_i	Length of the i-th heat exchanger (m)
U^i	Overall heat transfer coefficient (W/m^2 · K)
d^i_{in}, d^i_o	Diameters of inner and outer pipes (cm)
δ^i_{in}, δ^i_o	Thicknesses of inner and outer pipes (mm)
$\dot{m}^i_{wf}$	Working fluid mass flow rate (kg/s)
$\dot{m}_{req}$	Required fuel mass flow rate (kg/s)
$\dot{Q}^i_{load}$	Heat load from power system component (kW)
P^i_{wf}	Pressure of working fluid (bar)
$\Delta P^i_{H_2}$	Pressure drop of the fuel (bar)

Miscellaneous properties

χ_{tank}	Tank gravimetric index
$\chi_{tank,M}$	Maximum tank gravimetric index
χ	Overall gravimetric index
χ_M	Maximum overall gravimetric index at given P_{tank}
χ^*_M	Highest overall gravimetric index across all P_{tank}
E_Y	Young's modulus (N/m^2)
ν	Poisson's ratio

1. Introduction

The global aviation market is experiencing significant growth, but the associated rise in emissions poses a critical environmental challenge [1,2]. Aviation currently contributes a notable portion of global CO_2 and contrail emissions [3], making it imperative to develop revolutionary solutions to meet the industry's climate goals [4]. Hydrogen is a promising solution due to its clean combustion and a gravimetric energy density about 2.8 times higher than that of conventional aviation fuel, kerosene [5,6]. However, hydrogen's low density at ambient conditions (0.08 kg/m^3) presents major storage challenges, especially for long-haul flights. As a result, storing hydrogen in its saturated liquid form at 20 K, where its density increases to $\rho_{LH_2} = 70.8$ kg/m^3, has emerged as a practical approach for aviation applications. Recent efforts have explored various aspects of liquid hydrogen (LH_2) integration in aircraft, including structural sizing of cryogenic tanks, insulation strategies, pressure control mechanisms, and thermal management [6–13]. However, a holistic system that integrates LH_2 storage, thermal management, and transfer-control in a form scalable to aircraft design remains underexplored.

To fill this gap, the Integrated Zero Emission Aviation (IZEA) collaboration was launched to develop a comprehensive and scalable hydrogen-based propulsion system for future aircraft. As a first step, the project targets short-distance regional flights to evaluate the near-term feasibility of LH2-powered aviation. Central to this effort is a prototype hybrid-electric aircraft with a blended wing body configuration, designed to carry 100 passengers, as illustrated schematically in Fig. 1(a). Our analysis considers a flight power demand profile $\mathcal{P}_{dem}(t)$, as shown in Fig. 1(b), which includes the takeoff, cruising, and landing phases, spanning a total of 365 min [14]. An additional 100-min cruise fuel reserve is included in our analysis to account for potential delays or diversions. This aircraft is powered by a combination of hydrogen fuel cells and hydrogen-fueled combustion turbines driving high-temperature superconducting (HTS) electric generators. While hydrogen combustion is highly efficient in large gas turbines and HTS electric generators also provide excellent efficiency, NO_x emissions and contrails remain concerns that diminish hydrogen's otherwise positive impact on climate change and air quality [15,16]. Fuel cells offer a solution to avoid NO_x emissions and contrails, and several organizations (such as CHEETA [11,12] and Airbus [13]) are exploring fuel cell-powered aircraft. However, current fuel cell stacks remain too heavy to power a large aircraft through all mission phases, particularly during takeoff. The dual power source in the IZEA concept addresses this by using fuel cells during low-load conditions, such as taxiing and cruising—up to a maximum power of approximately 6.8 MW, as shown in Fig. 1(b)—while utilizing combustion turbine electric generators to supply the additional 9.4 MW power required during takeoff, bringing the total power to a peak of 16.2 MW. In addition, the dual power source enhances resiliency by providing power redundancy.

The LH_2 is stored in two storage tanks, symmetrically positioned around the aircraft's center axis, each equipped with a fuel transfer control system and connected to the corresponding power system components. From each storage tank, hydrogen flows through a series of

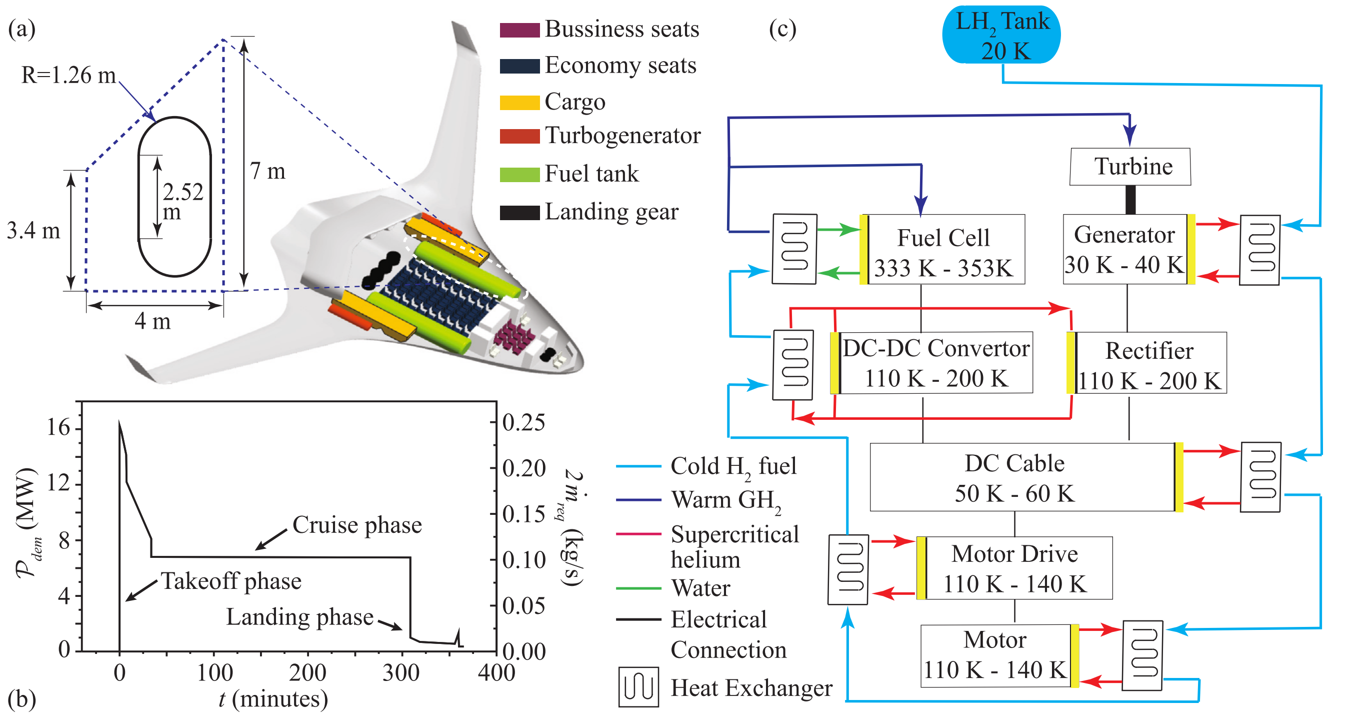

Fig. 1. (a) Layout of the blended wing-body airplane showing the space allocated for the liquid hydrogen fuel tank [14]. The inset displays the optimal tank geometry determined through the analysis presented in the text. (b) Flight power demand profile $\mathcal{P}_{dem}(t)$ for a short-range flight considered in our analysis. The corresponding required mass flow rate of hydrogen fuel $2\dot{m}_{req}(t)$ is also shown. (c) Schematic diagram illustrating hydrogen fuel flowing through heat exchangers associated with different power system components to provide cooling power before being fed into the fuel cell and combustion turboelectric generator.

heat exchangers, as illustrated in Fig. 1(c), before being supplied to the fuel cells and turboelectric generators. The working fluids in these heat exchangers are either supercritical helium or water, depending on the required operating temperature ranges and cooling demands of the power system components, as detailed in our later analysis. The electric power generated in the fuel cells and HTS generators is transmitted via HTS DC cables with near-zero resistive losses to power electronics, including DC-DC converters and generator rectifiers. The DC power is then converted back to AC power through motor drives, which power the aircraft's propellers to generate the necessary thrust.

This architecture is expected to have superior overall system efficiency. However, onboard LH_2 fuel storage must align with the aircraft's architecture and flight requirements [9,17–19]. Furthermore, managing the transfer of LH_2 to meet flight power demands while simultaneously addressing the cooling needs of power system components operating at different temperature ranges poses a significant design challenge [10,20,21]. In this paper, we present a comprehensive design for an LH_2 storage and transfer system integrated with the thermal management system of the proposed hybrid-electric aircraft. By regulating the pressure within the storage tanks, we demonstrate the feasibility of achieving the desired hydrogen mass flow rate while effectively cooling power system components using practical heat exchangers. Furthermore, we perform a system-level optimization of our design by maximizing an overall gravimetric index. The critical importance of this holistic optimization approach in determining optimal design parameters is discussed. This study represents a significant advancement in zero-emission aviation, promoting greater environmental sustainability.

2. Methods

The concept for our LH_2 storage, thermal management, and transfer-control system is illustrated in Fig. 2(a). We propose regulating the pressure inside the storage tank P_{tank} to supply hydrogen fuel at the mass flow rate $\dot{m}_{req}(t)$ required to meet the power demands of the flight. This approach avoids common issues associated with cryogenic pumps and cryofans used to drive LH_2 flow, including frictional heating from rotary components, LH_2 cavitation, seal failures, and hydrogen embrittlement [22]. Before reaching the fuel cells or combustion turbines, the hydrogen passes through a series of counterflow heat exchangers designed to provide the necessary cooling power to various power system components. The total pressure drop of the fuel across all the heat exchangers $\sum_i \Delta P^i_{H_2}$ vary with the fuel mass flow rate. Since fuel cells operate optimally at 1.3 bar [23], our goal is to maintain $P_{tank} = \sum_i \Delta P^i_{H_2} + 1.3$ bar during all flight phases. Tank pressure is controlled through two mechanisms: hydrogen gas charging and vapor venting. As shown in Fig. 2(a), a standard hydrogen gas cylinder equipped with a pressure regulator can be used to rapidly increase P_{tank}, while a vent valve can be controlled to release vapor and reduce P_{tank} (see details in Section 3.2). A pressure sensor continuously monitors the tank pressure, and feedback from the aircraft's power demands actuates the charging and venting processes.

Fig. 2(b) illustrates our iterative design flowchart for optimizing the key parameters of the LH_2 storage tanks and heat exchangers. The process begins by setting two input parameters: the vent pressure P_{vent} and the hold time τ_H. The vent pressure defines the maximum allowable tank pressure, beyond which vapor is vented through a leak valve, potentially routed to downstream heat exchangers to minimize fuel loss. The hold time represents how long the tank can store LH_2 without venting after refueling. Consider the typical pre-departure time of about 120 min for aircrafts before takeoff [24], we set $\tau_H = 120$ min in our analysis. As detailed in the next section, these two parameters allow us to determine the optimal tank and insulation configurations. Next, we design the heat exchangers to deliver the required cooling power to the power system components. Various configurations of heat exchanger geometry and working fluid properties can meet these requirements. We retain designs where the P_{tank} remains below P_{vent}, even during takeoff when

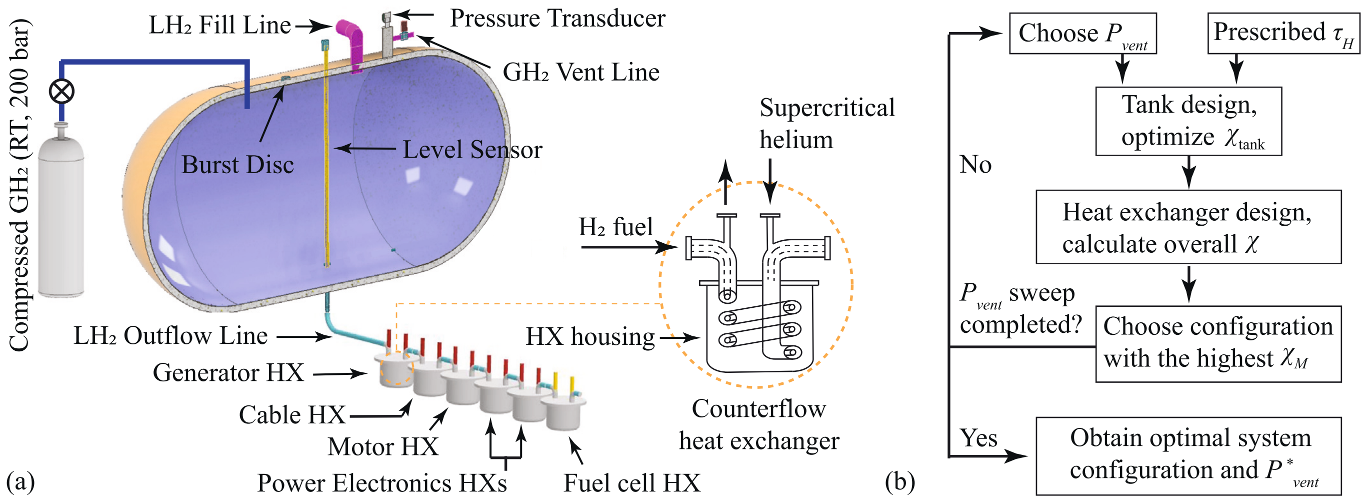

Fig. 2. (a) Schematic diagram showing the LH_2 storage tank (half-section), along with the heat exchangers through which hydrogen flows before reaching the fuel cells and the combustion turboelectric generators. The zoomed inset illustrates the counterflow heat exchanger for the generator. (b) Flowchart outlining the procedures for designing and optimizing the tank and thermal management systems.

maximum power demand and the highest mass flow rate occurs. After that, we calculate the overall gravimetric index χ, defined as the ratio of the initial LH_2 mass (m_{H_2}) in the tank to the combined mass of the fuel, storage tank, and the thermal management system, for each valid configuration. The design with the maximum gravimetric index (χ_M) is selected. Finally, we vary P_{vent} and repeat the process to identify χ_M for each P_{vent}, ultimately determining the optimal P^*_{vent} and the corresponding system parameters that yield the highest gravimetric index (χ^*_M). In what follows, we present the detailed design processes for the LH_2 tanks and the heat exchangers.

2.1. Tank design

Designing an efficient LH_2 storage system for aircraft involves challenges related to space constraints and weight optimization. The blended wing body airplane, illustrated in Fig. 1(a), offers an advantageous geometry for hydrogen aviation by providing increased space in the outer and rear fuselage compared to conventional commercial airplanes [6]. The designated area for the hydrogen storage tank is highlighted in the same figure. To estimate the required fuel mass and volume, we note the specific chemical energy of 120 MJ/kg released during the hydrogen oxidation reaction [6]. In fuel cells or turboelectric generators, this energy is converted into electricity with an average efficiency of around 50 % [6]. Based on the flight power demand profile $\mathcal{P}_{dem}(t)$ shown in Fig. 1(b), the required hydrogen mass flow rate from each tank can be calculated as: $\dot{m}_{req}(t) = \frac{1}{2}\mathcal{P}_{dem}(t)/(50\ \% \times 120\ \text{MJ/kg})$, which is also indicated in Fig. 1(b). By integrating $\dot{m}_{req}(t)$ over the entire flight duration and accounting for the 100-min cruise reserve, the total hydrogen mass is determined to be 2871.2 kg. With the hydrogen stored in two tanks, the fuel mass in each tank is $m_{H_2} = 1435.6$ kg, and the corresponding LH_2 volume is $V_{LH_2} = m_{H_2}/\rho_{LH_2} = 20.28\ \text{m}^3$.

To optimize the LH_2 tank design, we adopt the method developed by Winnefeld et al. to maximize the tank gravimetric index χ_{tank} [6], defined as $\chi_{tank} = m_{H_2}/(m_{H_2}+m_{wall}+m_{ins})$, where m_{wall} and m_{ins} denote the masses of the tank wall and insulation layer, respectively. To calculate χ_{tank}, it is necessary to determine the tank volume V, along with the material and thickness of both the wall (δ_w) and insulation layer (δ_{ins}). The workflow of this analysis is summarized in the flowchart in Fig. 3(a). The tank volume V can be determined as follows. Assume the tank is initially filled with LH_2 at $P_0 = 1$ bar to a liquid volumetric fraction y^0_l. After filling, the tank is closed, and any subsequent heat leakage causes the tank pressure P_{tank} to rise. In this closed system, where both the fuel mass and tank volume remain constant, the liquid volume fraction $y_l(P)$ at any elevated pressure P can be determined by solving:

$$\frac{y_l(P)}{v_l(P)} + \frac{1-y_l(P)}{v_g(P)} = \frac{y^0_l}{v_l(P_0)} + \frac{1-y^0_l}{v_g(P_0)}, \tag{1}$$

where $v_l(P)$ and $v_g(P)$ are the specific volumes of saturated liquid and vapor hydrogen, respectively [6]. Fig. 3(b) shows a set of $y_l(P)$ curves corresponding to different initial fill fractions y^0_l. To prevent LH_2 from spilling through the fill port, we set the vent pressure P_{vent} to be the tank pressure at which y_l reaches 97 %, ensuring that vapor vents without further increasing the liquid level [6]. As a consequence, P_{vent} is directly related to the initial fill fraction y^0_l (see Fig. 3(b)): a higher y^0_l corresponds to a lower P_{vent}, and vice versa. Given a specific input P_{vent}, the required tank volume can thus be calculated as $V = V_{LH_2}/y^0_l$.

Next, following recommendations from NASA [7] and other studies [8,25], we select aluminium alloy 2219 (Al-2219) as the tank wall material. This alloy is widely used for cryogenic applications, offering relatively low density of $\rho_w = 2825\ \text{kg/m}^3$ and a high limit stress of $K = 172.4$ MPa at 20 K [6]. To evaluate the tank wall thickness δ_w for calculating m_{wall}, we need to specify the tank geometry, since δ_w depends on both the maximum tank pressure (i.e., P_{vent}) and the local curvature of the tank wall. Following Winnefeld et al. [6], we model the tank as an elliptical shell with two half-ellipsoid end caps, as illustrated in Fig. 3(c). This tank geometry can be described by four shape parameters: the length of the shell section l_s, the major radius a and minor radius c of the shell's elliptical cross section, and the height of the half-ellipsoidal end caps which is set equal to c [6]. Given the tank volume constraint $V = (4/3)\pi ac^2 + \pi acl_s$, one only needs two dimensionless ratio parameters to describe the tank geometry: $\phi = a/c$ and $\lambda = l_s/(l_s + 2\,c)$. In our analysis, we vary ϕ from 0.5 to 1.5 and λ from 0.1 to 0.9, then calculate δ_w for each shape configuration for both the elliptical shell and the end caps based on curvature and P_{vent} using established correlations reported in Refs. [6,26]. With δ_w determined, the tank mass m_{wall} can be calculated.

For insulation, Mital et al. conducted a comprehensive review of various insulation strategies, including foam, aerogels, vacuum with multilayer insulation (MLI), vapor-cooled shields, composite materials, and their combinations [7]. Vacuum-based insulation minimizes heat leakage but requires a sealed double-wall tank to maintain the vacuum, adding significant mass that negatively impacts aircraft performance and operating costs [27–29]. Additionally, vacuum loss presents a

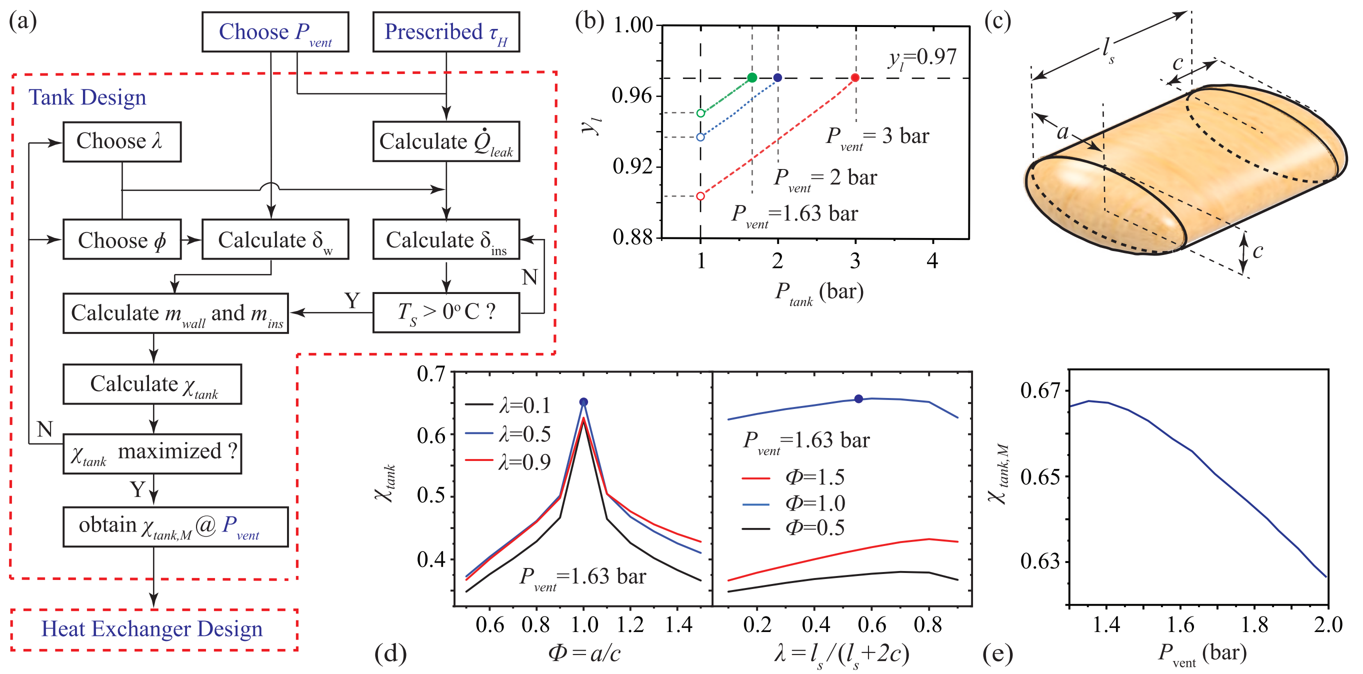

Fig. 3. (a) Flowchart showing the steps for LH_2 tank design. (b) Liquid volume fraction y_l in a closed LH_2 tank as a function of the tank pressure P_{tank} following initial filling at 1 bar. (c) Shape parameters a, c, l_s defining the tank geometry. (d) Variations of the tank gravimetric index χ_{tank} with the tank's geometrical ratio parameters at $P_{vent} = 1.63$ bar. The maximum value $\chi_{tank,M}$ is marked by the solid circles. (e) The obtained $\chi_{tank,M}$ at different input parameter P_{vent}.

catastrophic safety risk during flight [29]. Aerogel insulation also offers low heat leakage, but its poor mechanical properties and material performance uncertainties currently limit its aviation applications [7,30]. Composite materials, such as carbon or glass fiber reinforced polymers, provide high strength and notable weight savings, but hydrogen permeation and microcracking remain challenges [7]. While metallic liners can help mitigate permeation, they introduce issues such as thermal expansion mismatches between layers [31,32]. On the other hand, closed-cell rigid polyurethane foam is widely favored in LH_2 storage designs due to its low weight, adequate thermal conductivity for short- to medium-range flights, and high technology readiness level [6,25]. In our analysis, we apply this insulation externally to the tank wall.

The insulation thickness, δ_{ins}, is selected based on the following considerations. After the tank is filled with LH_2, heat leakage from the ambient environment at $T_0 = 293$ K will cause the tank pressure to rise. The insulation thickness should be chosen to limit the heat leak rate, $\dot{Q}_{leak}$, so that over the standby period, $\tau_H = 120$ min, P_{tank} does not exceed the vent pressure P_{vent}. This approach minimizes fuel loss from venting while the aircraft is on the ground before takeoff. Let E_i be the initial internal energy of the LH_2 after filling, and E_f be the internal energy when the tank pressure reaches P_{vent}. The maximum allowable heat leak rate can then be expressed as $\dot{Q}_{leak} = (E_f - E_i)/\tau_H$. To achieve this target heat leak rate, the minimum required insulation thickness δ_{ins} can be calculated as follows [33]:

$$\delta_{ins} = \frac{A}{\dot{Q}_{leak}} \int_{20\,\mathrm{K}}^{T_s} k_{ins}(T)\, dT \tag{2}$$

where T_s is the insulation outer surface temperature, A is the tank surface area which can be calculated for the given tank geometry, and $k_{ins}(T)$ is the temperature-dependent thermal conductivity of polyurethane foam [34]. The value of T_s is determined based on air convection over the insulation surface: $\dot{Q}_{leak} = h_{air} A (T_0 - T_s)$, where the heat transfer coefficient h_{air} for air at ambient temperature T_0 is evaluated using the standard Nusselt number correlation for natural convection on a horizontally oriented tank [35]. If T_s is found to be below 273 K, we will increase δ_{ins} to reduce $\dot{Q}_{leak}$, ensuring T_s remains above 273 K to prevent ice forming on the insulation surface.

With δ_w and δ_{ins} established, we calculate m_{wall} and m_{ins}, obtaining χ_{tank} for each tank configuration. The calculated χ_{tank} values for various tank configurations at $P_{vent} = 1.63$ bar are shown in Fig. 3(d). The results indicate that the maximum $\chi_{tank,M}$ is achieved for a tank with aspect ratios $\phi = 1$ and $\lambda \simeq 0.55$, consistent with findings of Winnefeld et al. [6]. Since χ_{tank} varies mildly with λ, this parameter can be adjusted around 0.5 if space constraints limit tank placement. In Fig. 3(e), we show the maximum $\chi_{tank,M}$ obtained at different P_{vent}. The results suggest that the highest $\chi^*_{tank,M} \simeq 0.67$ is achieved at a vent pressure $P^*_{vent} = 1.36$ bar. However, as will be shown later, when a system-level optimization is performed to maximize the overall gravimetric index, the optimal P_{vent} shifts to 1.63 bar.

2.2. Heat exchanger design

Some power system components, particularly the superconducting ones such as the HTS electric generators and DC cables, can achieve exceptionally high efficiencies. Nonetheless, they still generate heat due to AC losses and other dissipation mechanisms [36–38]. Table 1 provides the estimated typical efficiencies η^i and operating temperatures for the primary power system components [14,39]. Based on the power demand profile shown in Fig. 1(b), the peak power requirement during takeoff is about $\mathcal{P}_{dem} = 16.2$ MW. Since the airplane has two identical power system architectures on its two sides, each system handles a peak power of 8.1 MW. In normal operation, the fuel cells contribute 3.4 MW per side, matching the cruise-phase power demand shown in Fig. 1(b), while the HTS generators supply the remaining 4.7 MW per side during takeoff. However, for thermal load evaluation and heat exchanger design, we conservatively assume a full 8.1 MW output from the HTS generators to account for a potential scenario in which the fuel cell system is non-operational due to a fault or other issue. This assumption reflects our power redundancy strategy and ensures that the generator-side heat exchangers can manage the full thermal load under worst-case conditions. Consequently, the peak heat generation rate for each power

Table 1
Heat exchanger label (i), estimated efficiency (η^i), operating temperature (T^i), and peak heat load ($\dot{Q}^i_{\mathrm{load}}$) for the power system components.

i	Component	η^i (%)	T^i (K)	$\dot{Q}^i_{\mathrm{load}}$ (kW)
1	HTS generator	99.9	30–40	8.1
2	HTS DC cable	99.9	50–60	8.1
3	Motor	99.2	110–140	65.3
4	Motor drive	99.0	110–140	81.8
5	DC-DC converter and rectifier	99.0	110–200	81.8
6	Fuel cells	~50	333–353	3400

system component is estimated as $\dot{Q}^i_{load} = (1 - \eta^i) \times (P^i/\eta^i)$ MW, where $P^i = 3.4$ MW for the fuel cells and 8.1 MW for all other components. The corresponding results are summarized in Table 1.

To cool the components, one possible approach would be to divert a fraction of the cold hydrogen fuel directly through each component. However, this method couples component thermal loads to the fuel flow, making it difficult to independently control component temperatures. It also poses significant practical challenges, including material compatibility with cryogenic hydrogen, risks of embrittlement and thermal shock during transients, and added safety concerns due to hydrogen's high diffusivity and flammability, which complicate leak prevention and fault isolation in distributed systems. To avoid these issues, we instead equip each component with a dedicated circulation loop to transfer heat to the cold hydrogen fuel, as illustrated in Fig. 1(c). This design enables independent thermal management by controlling the flow within each loop without affecting the performance of other components. For components labeled $i = 1$–5 in Table 1, we use supercritical helium as the working fluid due to its proven efficacy within the required temperature range [40–42]. Each circulation loop includes two heat exchangers: one connected to the hydrogen fuel pipeline and the other to the power system component. The design of the latter depends on the specific geometry and materials of each power system component, details of which are not currently available. Therefore, this study focuses on designing the heat exchangers that interface directly with the hydrogen fuel pipeline.

The combustion turbines and fuel cells operate at lower efficiencies. For instance, fuel cells can typically achieve a maximum efficiency of around 50 % when operated at 1.3 bar and within a temperature range of 333–353 K [23]. This limited efficiency results in substantial heat generation in the fuel cells, necessitating innovative cooling strategies to maintain their optimal operating conditions. One possible approach involves transferring this heat to the aircraft's surface, allowing it to be dissipated by the cold air flowing over it [43]. This skin-cooling concept, while promising, is beyond the scope of the current work. Nonetheless, in this study we incorporate a heat exchanger ($i = 6$) between the fuel pipeline and the fuel cell stack using water as the working fluid, allowing us to utilize the waste heat to preheat the hydrogen fuel to 333 K, supporting optimal fuel-cell operation.

As shown in Fig. 2(a), we adopt pipe-in-pipe counterflow heat exchangers placed in protective housing. The counterflow configuration is chosen for its high thermal effectiveness and simplicity [44], allowing us to establish a baseline framework for system-level analysis. While compact designs such as plate-and-fin exchangers may offer reduced length, they introduce added structural complexity and mass that require detailed trade-off analysis, which we are pursuing in ongoing work. The present analysis begins by evaluating the inlet and exit temperatures of the hydrogen fuel and the working fluid for each heat exchanger. As LH_2 flows out of the storage tank at a mass flow rate $\dot{m}_{req}$, the heat load required to fully vaporize it is given by $\dot{Q}_{fg} = \dot{m}_{req} H_{fg}$, where $H_{fg} = 448$ kJ/kg is the specific enthalpy of vaporization for hydrogen around 1 bar. At the peak mass flow rate, $\dot{Q}_{fg}$ is about 56.1 kW, which is greater than the combined heat loads from the HTS generator and DC cables, according to Table 1. Therefore, the hydrogen fuel remains as a liquid–vapor mixture while passing through heat exchangers $i = 1, 2$, with its inlet and exit temperatures both at the saturation temperature of about 20 K. For heat exchangers $i = 3$–5, the specific enthalpy of the fuel at the exchanger exit can be calculated as: $H^i_{H_2,ex} = H_{LH_2} + (\sum_{n=1}^{i} \dot{Q}^n_{load})/\dot{m}_{req}$, where H_{LH_2} is the specific enthalpy of LH_2 in the storage tank. In the pressure range considered, the specific enthalpy of the hydrogen fuel is nearly solely correlated with its temperature [45], allowing us to determine the exit temperature of the fuel $T^i_{H_2,ex}$. The inlet temperature of the fuel at the i-th heat exchanger $T^i_{H_2,in}$ is taken as the exit temperature of the preceding exchanger $T^{i-1}_{H_2,ex}$. This treatment is valid because the heat leak in the fuel pipeline between exchangers is designed to be negligible compared to the heat loads listed in Table 1. For heat exchanger $i = 6$, the fuel exit temperature is set to 333 K, and the heat load $\dot{Q}^6_{load} = \dot{m}_{req}[H^6_{H_2,ex}(333\text{ K}) - H^6_{H_2,in}] \simeq 311$ kW replaces the value listed in Table 1.

For the working fluid in the heat exchangers, the inlet temperature $T^i_{wf,in}$ and exit temperature $T^i_{wf,ex}$ are set to the upper and lower bounds of the operating temperature range for the corresponding power system component, as listed in Table 1. As for their working pressures, $P^i_{wf} = 20$ bar is set for supercritical helium in heat exchangers $i = 1$–5, considering cryofan selection requirements, as will be discussed later. For heat exchanger $i = 6$, a water pressure of 1 bar is assumed. With the inlet and exit states of the working fluids known for each heat exchanger, the specific enthalpy $H^i_{wf,in}$ and $H^i_{wf,ex}$ can be determined. Using these specific enthalpy values, the required mass flow rate of the working fluid in each circulation loop can be calculated as: $\dot{m}^i_{wf} = \dot{Q}^i_{load}/(H^i_{wf,in} - H^i_{wf,ex})$. This analysis ensures that each heat exchanger can accommodate the peak thermal load during takeoff. In subsequent phases, such as cruising, the working fluid flow rates in each heat exchanger loop are adjusted according to the power demands. The flow rate in the HTS generator loop can be reduced to a minimal level sufficient to maintain superconducting conditions, allowing for rapid reactivation if needed.

Next, we proceed to determine the dimensions of each heat exchanger, following the steps outlined in the flowchart in Fig. 4. The process begins with selecting the diameters of the inner pipe d^i_{in} and the concentric outer pipe d^i_o for the pipe-in-pipe heat exchangers $i = 1$–6. The hydrogen fuel flows through the inner pipe, while the working fluid flows in opposite direction within the annulus formed between the two pipes. To determine the length of the i-th heat exchanger L_i, we use the heat transfer equation: $\dot{Q}^i_{load} = U^i A_i \Delta T^i_{lm}$, where U^i is the overall

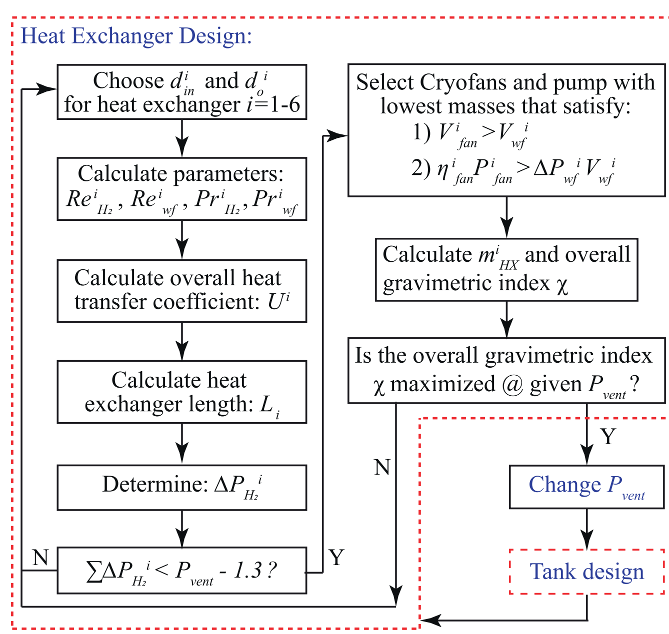

Fig. 4. Flowchart showing the steps for designing the heat exchangers.

heat transfer coefficient, $A_i = \pi d^i_{in} L_i$ is the heat transfer surface area, and $\Delta T^i_{lm} = (\Delta T^i_{ex} - \Delta T^i_{in})/\ln(\Delta T^i_{ex}/\Delta T^i_{in})$ is the log mean temperature difference [46], with ΔT^i_{ex} and ΔT^i_{in} being the temperature differences between the fuel and the working fluid at the inlet and exit, respectively. This equation allows us to calculate L_i once U^i is determined.

The value of U^i depends on the convective heat transfer coefficients of the fuel $h^i_{H_2}$ and the working fluid h^i_{wf} as $(U^i)^{-1} = (h^i_{H_2})^{-1} + (h^i_{wf})^{-1}$. These coefficients can be calculated using their respective Nusselt numbers [35]: $h^i_{H_2} = k^i_{H_2} Nu^i_{H_2}/d^i_{in}$ and $h^i_{wf} = k^i_{wf} Nu^i_{wf}/(d^i_o - d^i_{in})$, where the Nusselt numbers are obtained using the Chilton–Colburn correlation [46], based on the Reynolds and Prandtl Numbers for the fuel ($Re^i_{H_2} = \rho^i_{H_2} u^i_{H_2} d^i_{in}/\mu^i_{H_2}$ and $Pr^i_{H_2} = \mu^i_{H_2} C^i_{p,H_2}/k^i_{H_2}$) and the working fluid ($Re^i_{wf} = \rho^i_{wf} u^i_{wf}(d^i_o - d^i_{in})/\mu^i_{wf}$ and $Pr = \mu^i_{wf} C^i_{p,wf}/k^i_{wf}$). The physical properties in the expressions of the Reynolds and Prandtl numbers (see the Nomenclature for definitions) are evaluated at the average temperatures of the fuel and working fluids across each respective heat exchanger. We have also conduced finite element analysis using properties based on local temperatures and confirmed that the results show negligible differences. The mean flow velocities of the fuel $u^i_{H_2}$ and the working fluid u^i_{wf}, required for the Reynolds number calculations, can be determined from their respective mass flow rates as: $u^i_{H_2} = \dot{m}_{req}/(\rho^i_{H_2} \pi {d^i_{in}}^2/4)$ and $u^i_{wf} = \dot{m}^i_{wf}/[\rho^i_{wf} \pi({d^i_o}^2 - {d^i_{in}}^2)/4]$. With the obtained U^i, the length L_i of each heat exchanger for the chosen diameters d^i_{in} and d^i_o can be determined.

The geometry of the heat exchangers obtained through the above analysis ensures effective management of the heat loads from the power system components. However, we also need to make sure the tank pressure, regulated as $P_{tank} = \sum_{i=1}^{6} \Delta P^i_{H_2} + 1.3$ bar, always remains below the maximum allowable tank pressure P_{vent}, even during peak fuel demand at takeoff. For this purpose, we need to evaluate the pressure drop $\Delta P^i_{H_2}$ of the fuel across each heat exchanger. For heat exchangers $i = 1, 2$ and part of $i = 3$, where the fuel exists as a liquid–vapor mixture, the pressure drop can be evaluated using the correlation for two-phase pipe flows [47]:

$$\Delta P^i_{H_2} = \frac{f^i_{H_2} \dot{m}^2_{req} L_i}{2\rho^i_{H_2} A_i^2 \, d^i_{in}} \frac{1}{x^i_{H_2,ex} - x^i_{H_2,in}} \int_{x^i_{H_2,in}}^{x^i_{H_2,ex}} \phi_l^2(x_{H_2})\, dx_{H_2} \tag{3}$$

where $f^i_{H_2} = [0.79 \ln(Re^i_{H_2}) - 1.64]^{-2}$ is the friction factor for turbulent flows in smooth pipes [46], and $x^i_{H_2,in}$ and $x^i_{H_2,ex}$ are the quality factors of the fuel at the inlet and exit of the heat exchanger i, respectively. These quality factors can be determined based on the corresponding specific enthalpy, $H^i_{H_2,in}$ and $H^i_{H_2,ex}$. In the above expression, $\phi_l^2(x_{H_2})$ is the two-phase friction multiplier, which depends on the fuel quality factor x_{H_2} as [47]:

$$\phi_l^2(x_{H_2}) = \left[1 + x_{H_2}\left(\frac{\rho_{LH2}}{\rho_{GH2}} - 1\right)\right]\left[1 + x_{H_2}\left(\frac{\mu_{LH2}}{\mu_{GH2}} - 1\right)\right]^{-0.25} \tag{4}$$

where ρ_{GH_2} is saturated hydrogen vapor density at 20 K, and μ_{LH_2} and μ_{GH_2} are the dynamic viscosity of liquid and gaseous hydrogen at 20 K, respectively. In the remaining part of heat exchanger $i = 3$ and for heat exchangers $i = 4$–6, where the fuel exists as a pure gas, the pressure drop can be calculated using the expression for single-phase flows [48]: $\Delta P^i_{H_2} = (1/2)\rho^i_{H_2} f^i_{H_2} L^i {u^i_{H_2}}^2/d^i_{in}$. If the condition $\sum_{i=1}^{6} \Delta P^i_{H_2} \le P_{vent} - 1.3$ bar is not satisfied, the case will be discarded, the diameters d^i_{in} and d^i_o will be adjusted, and the analysis will be repeated until the condition is fulfilled.

The next step is to select the cryofans and pump to drive the working fluids in the circulation loops. This selection is based on two criteria. The first one is that the maximum flow capacity of the cryofan or pump, $\dot{V}^i_{fan}$, must exceed the volumetric flow rate $\dot{V}^i_{wf}$ of the working fluid. For heat exchangers $i = 1$–5, $\dot{V}^i_{wf}$ for supercritical helium is given by $\dot{V}^i_{wf} = \dot{m}^i_{wf}/\rho^i_{wf}$, where the helium density ρ^i_{wf} can be adjusted by varying its pressure P^i_{wf}. We consider all the cryofan models from Stirling Cryogenics [49], a leading provider in the field. These cryofans typically have a maximum operating pressure in the range of 20 to 30 bar, and the models with higher $\dot{V}^i_{fan}$ generally have larger impellers and hence greater masses. To minimize the weight of the cryofans, we opt to operate supercritical helium at $P^i_{wf} = 20$ bar, ensuring a high ρ^i_{wf} and hence a low $\dot{V}^i_{wf}$. For heat exchanger $i = 6$, water is circulated at $P^6_{wf} = 1$ bar, whose density and hence $\dot{V}^6_{wf}$ can be readily determined to guide the selection of the water pump. The second criteria is that the power capacity, $\mathcal{P}^i_{fan}$, of the cryofans and the pump must be sufficient to maintain the required mass flow rate, $\dot{m}^i_{wf}$, of the working fluid. The power needed to drive the working fluid flow is given by $\dot{V}^i_{wf} \Delta P^i_{wf}$, where $\Delta P^i_{wf} = (1/2)\rho^i_{wf} f^i_{wf} L^i {u^i_{wf}}^2/(d_o - d_{in})$ is the pressure drop of the working fluid across the heat exchanger i. Therefore, the second criterion can be expressed as $\eta^i_{fan}\mathcal{P}^i_{fan} > \dot{V}^i_{wf}\Delta P^i_{wf}$, where η^i_{fan} is the efficiency of the cryofans or pump, as specified by Stirling Cryogenics [49]. In our design, we select the cryofan with the lowest mass for each heat exchanger loop that satisfies both criteria.

After obtaining all the design parameters of the heat exchanger system, we proceed to calculate the overall gravimetric index χ for a system level optimization:

$$\chi = m_{H_2} \Big/ \left(m_{H_2} + m_{wall} + m_{ins} + \sum_{i=1}^{6} m^i_{HX} \right), \tag{5}$$

where m^i_{HX} denotes the total mass of the i-th heat exchanger system, which includes the mass of the heat exchanger body $m^i_{HX,bd}$, the mass of the heat exchanger insulation $m^i_{HX,ins}$, the mass of the cryofan (or pump) $m^i_{HX,fan}$, and the mass of the working fluid within the heat exchanger $m^i_{HX,wf}$. The latter two contributions can be readily determined based on the geometry of heat exchangers, densities of the working fluids, and the cryofans and pump information from the vendor. To calculate $m^i_{HX,bd}$, we need to determine the thickness of the inner and outer pipes. The outer pipes are internally pressurized by the working fluids (i.e., $P^i_{wf} = 20$ bar for $i = 1$–5 and $P^i_{wf} = 1$ bar for $i = 6$). Following established convention [50], we set the outer pipe thickness as $\delta^i_o = P^i_{wf} d^i_o/2\ K$, where K is the limiting stress of the outer pipe material, chosen to be aluminium alloy Al-2219 [51]. The inner tube is typically subjected to external pressurization as the fuel pressure is lower than P^i_{wf}. Its thickness can be calculated as [51]: $\delta^i_{in} = d^i_{in}[P^i_{wf}(1 - \nu^2)/2E_Y]^{1/3}$, where ν is the Poisson's ratio and E_Y is the Young's modulus of the pipe material, Al-2219 [51]. For heat exchangers i =1-5, we apply a polyurethane insulation layer to the outer surface to limit the ambient heat leak rate into the heat exchanger to less than 5 % of $\dot{Q}^i_{load}$. The required insulation thickness can be determined through a similar analysis as depicted by Eq. (2), which allows the calculation of $m^i_{HX,ins}$.

For a given P_{vent}, there are many valid designs of the heat exchanger system. We systematically varying d^i_{in} and d^i_o to explore all the valid design configurations. Among these, the one with the highest overall gravimetric index, χ_M, is retained. We then adjust P_{vent} and repeat the tank and heat exchanger design processes to determine the dependence of χ_M on P_{vent}.

3. Results and discussion

3.1. System optimization analysis results

In Fig. 5, we present the obtained χ_M as a function of P_{vent}, along with additional curves illustrating how the inclusion of various components in the total mass impacts the value of χ_M. When the total mass includes only the fuel and the tank system, the highest gravimetric index, $\chi^*_M = 0.67$, is achieved at an optimal vent pressure of $P^*_{vent} = 1.36$ bar. Adding the masses of the heat exchanger body and insulation shifts the optimal P^*_{vent} to 1.58 bar. This shift arises because, at relatively low P_{vent}, although the tank benefits from a reduced mass due to the thinner required wall thickness, the lower pressure within the tank limits the

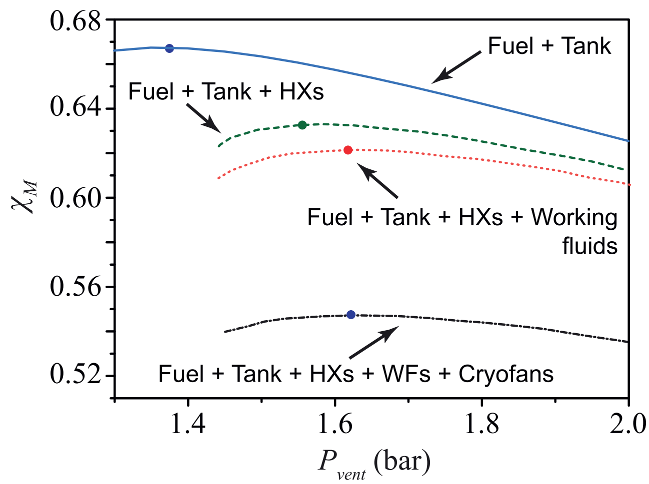

Fig. 5. Maximum overall gravimetric index, χ_M, as a function of the design parameter P_{vent}. For comparison, χ_M curves for analyses based on different contributions to the total mass are included.

achievable pressure head from the tank to the fuel cell stacks. Due to this constraint, all heat exchangers must be designed with larger diameters to maintain sufficiently small pressure drops $\Delta P^i_{H_2}$. Consequently, the size and total mass of the heat exchanger systems increase significantly, ultimately reducing the overall gravimetric index at low P_{vent}. Further shift of P^*_{vent} to 1.63 bar occurs when the masses of the working fluids are included, and the corresponding $\chi^*_M = 0.62$. This progression demonstrates the necessity of system-level optimization to determine the best design parameters. In contrast, adding the cryofan masses results in a uniform scaling down of the χ_M curve without altering the optimal P^*_{vent}. This behavior occurs because the optimal cryofan models remain unchanged across the explored range of P_{vent}. Similarly, incorporating other aircraft component masses that are independent of P_{vent}, such as heat exchanger protective housing, would also rescale the curve without affecting P^*_{vent}.

For the optimal configuration achieved at $P^*_{vent} = 1.63$ bar, the mass fractions of the system components are as follows: fuel (54.7 %), tank wall (25.4 %), tank insulation (3.2 %), heat exchangers and insulation (3.4 %), working fluids (1.4 %), and cryofans and water pump (11.9 %). The resulting tank geometry is illustrated in Fig. 1(a), which has a wall thickness of $\delta_W = 7.3$ mm and an insulation thickness of $\delta_{ins} = 7.5$ cm, fitting nicely within the outer and rear fuselage of the aircraft. The heat exchanger parameters for the optimal configuration are listed in Table 2, along with the pressure drop $\Delta P^i_{H_2}$ of the fuel across each heat exchanger at the peak mass flow rate during takeoff. Notably, the inner diameter of the fuel pipeline, d^i_{in}, increases from 3.8 cm or less for heat exchangers $i = 1$–2 to over 5 cm for heat exchangers $i = 3$–6. This increase is necessitated by the transition of LH_2 to vapor in heat exchanger $i = 3$, resulting in a significant drop in fuel density that becomes more pronounced as the fuel temperature rises in the subsequent heat exchangers. At a given $\dot{m}_{req}$, the lower density leads to a higher mean velocity of the fuel in the pipeline. To maintain a manageable pressure drop $\Delta P^i_{H_2}$, a larger d^i_{in} is then required.

In Table 3, we list the models and specifications of the cryofans and water pump selected to drive the working fluids in the heat exchangers for the optimal design configuration. The table also includes the derived parameters of the working fluids in these heat exchangers. For heat exchangers $i = 1$–2, the Chinook cryofan is identified as the optimal choice due to its lightweight design (weighing only 8 kg) and its ability to deliver the required volumetric flow rate and power output [49]. For heat exchangers $i = 3$–5, the Tramontana cryofan is selected, despite its larger mass of 90 kg. This selection is necessary to meet both the increased volume flow rate of the working fluid $\dot{V}^i_{wf}$ and the higher power demand $\dot{V}^i_{wf}\Delta P^i_{wf}$ required to drive the working fluids in these heat exchangers. The data in Table 3 also show that the maximum power output of each cryofan $\eta^i_{fan}\mathcal{P}^i_{fan}$ is significantly higher than the power demand for driving the working fluid. This is advantageous, as the selected cryofans may have sufficient power to maintain the same mass flow rate, even if a second heat exchanger is added to each circulation loop in the future to transfer heat from the power system component to the working fluid. Water circulation for preheating the hydrogen fuel using waste heat from the fuel cell stacks is achieved with a commercially available Magnatex pump [52], which meets both the volumetric flow capacity and power requirements.

3.2. Tank pressure regulation

As discussed earlier, the tank pressure must be regulated during flight as $P_{tank} = \sum_{i=1}^{6}\Delta P^i_{H_2} + 1.3$ bar in order to maintain the required fuel mass flow rate $\dot{m}_{req}(t)$ to meet the power demands $\mathcal{P}_{dem}(t)$. The calculated $P_{tank}(t)$ profile for the optimal configuration, based on the $\mathcal{P}_{dem}(t)$ profile shown in Fig. 1, is illustrated in Fig. 6. This profile includes a 40-min taxi-out period, during which P_{tank} increases from 1 bar immediately after fuel refilling to about 1.2 bar due to heat leakage through the tank insulation. Prior to takeoff at $t = 0$, P_{tank} must be ramped up to above 1.6 bar in order to meet the takeoff power demand. This can be achieved by charging the tank with room-temperature hydrogen gas from the compressed hydrogen cylinder, as illustrated in Fig. 2. If the charging pressure is regulated to 10 bar through a charging pipeline with a diameter of 0.25 inches and a length of 2 m, it is estimated that P_{tank} can be increased from 1.2 bar to 1.63 bar in less than half a minute. In urgent situation, such as when a go-around is required during landing, the power $\mathcal{P}_{dem}(t)$ must be ramped up rapidly from minimal to peak levels. In such cases, the charging pressure can be increased to a much higher level, such as 200 bar, allowing P_{tank} to reach its peak value within a few seconds.

Following the climb phase, P_{tank} needs to be reduced as the power demand $\mathcal{P}_{dem}$ decreases. Once the gas charging process is complete, the outflowing LH_2 at the required mass flow rate $\dot{m}_{req}$ naturally decreases P_{tank}. Conversely, the ambient heat leakage through the hydrogen tank wall $\dot{Q}_{leak}$ vaporizes LH_2, leading to an increase in P_{tank}. To control P_{tank} and ensure it follows the required profile as shown in Fig. 6 for $t > 0$, some hydrogen vapor must be released from the tank using a controlled vent valve. The vapor venting mass flow rate $\dot{m}_v$ can be determined by evaluating the rate of change of the total fuel mass $\dot{m}_{H_2}$ and internal energy $\dot{E}_{H_2}$ in the storage tank as follows:

Table 2
Heat exchanger specifications for the optimal design configuration that achieves the highest overall gravimetric index at $P^*_{vent} = 1.63$ bar.

i	Component	Working fluid	$\dot{m}^i_{wf}$ (kg/s)	P^i_{wf} (bar)	d^i_{in} (cm)	δ^i_{in} (mm)	d^i_o (cm)	δ^i_o (mm)	L^i (m)	$\delta^i_{ins,HX}$ (cm)	$m^i_{HX,bd} + m^i_{HX,ins}$(kg)	$\Delta P^i_{H_2}$ (kPa)
1	Generator	SHe	0.15	20	3.32	0.76	4.17	1.21	4.03	1.34	3.04	1.07
2	Cable	SHe	0.15	20	3.81	0.87	4.78	1.38	1.83	0.59	1.67	0.57
3	Motor	SHe	0.41	20	5.23	1.20	6.55	1.89	4.82	0.22	8.09	1.03
4	Motor drive	SHe	0.52	20	5.72	1.31	7.77	2.26	9.55	0.42	21.59	5.36
5	Converter/rectifier	SHe	0.17	20	6.50	1.49	8.13	2.36	19.24	0.94	51.20	14.13
6	Fuel cell	Water	3.49	1	7.32	0.21	9.12	0.21	13.37	0	4.13	10.65

Table 3
Specifications of the cryofans and pump used to drive the working fluids in the heat exchangers for the optimal design configuration at P^*_{vent} = 1.63 bar. Parameters of the working fluids in these heat exchangers are also provided.

i	Component	Model of cryofan/pump	$m^i_{HX,fan}$ (kg)	$\dot{V}^i_{fan}$ (m^3/s)	$\mathcal{P}^i_{fan}$ (W)	η^i_{fan} (%)	P^i_{wf} (bar)	$\dot{m}^i_{wf}$ (kg/s)	$\dot{V}^i_{wf}$ (m^3/s)	$\dot{V}^i_{wf}\Delta P^i_{wf}$ (W)
1	Generator	Chinook	8	0.0094	120	71	20	0.15	0.005	55.66
2	Cable	Chinook	8	0.0094	120	71	20	0.15	0.008	37.33
3	Motor	Tramontana	90	0.083	2400	90	20	0.41	0.054	1939.84
4	Motor drive	Tramontana	90	0.083	2400	90	20	0.52	0.068	1429.74
5	Converter/rectifier	Tramontana	90	0.083	2400	90	20	0.17	0.028	395.46
6	Fuel cell	Magnatex	26	0.005	2238	–	1	3.49	0.0035	55.61

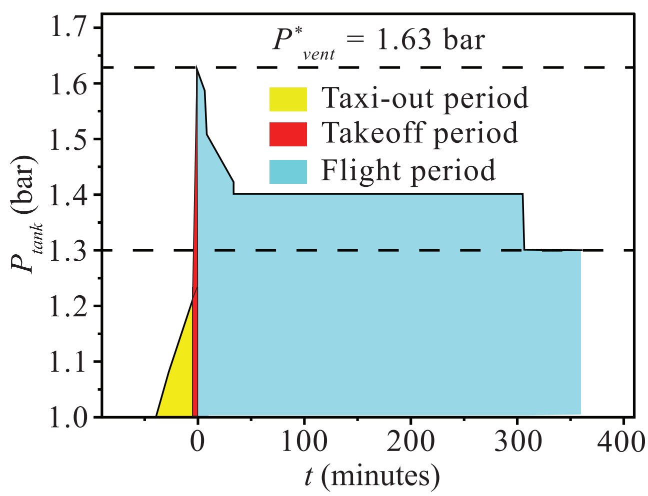

Fig. 6. Calculated tank pressure P_{tank} required to deliver fuel and meet the power demand shown in Fig. 1(a), using the optimal tank and heat exchanger configuration. A 40-min taxi-out period is included.

$$\dot{m}_{H_2} = \frac{d}{dt}\left[y_l(t)\rho_{LH_2}V + (1-y_l(t))\rho_{GH_2}V\right] = -\dot{m}_{req}(t) - \dot{m}_v(t), \tag{6}$$

$$\dot{E}_{H_2} = \frac{d}{dt}\left[y_l(t)\rho_{LH_2}V\mathcal{E}_{LH_2} + (1-y_l(t))\rho_{GH_2}V\mathcal{E}_{GH_2}\right] = \dot{Q}_{leak} - \dot{m}_{req}(t)H_{LH_2} - \dot{m}_v(t)H_{GH_2}, \tag{7}$$

where H_{GH_2} is the specific enthalpy of saturated hydrogen vapor at 20 K, while $\mathcal{E}_{LH_2}$ and $\mathcal{E}_{GH_2}$ denote the specific internal energies of saturated liquid and vapor hydrogen at 20 K, respectively. The rate of heat leakage $\dot{Q}_{leak}$ for the optimal tank configuration is shown in Fig. 7(a). Its time variation corresponds to changes in flight altitude. On the ground, with an ambient temperature of 20 °C, $\dot{Q}_{leak}$ is about 3.45 kW. At cruising altitude, where the ambient temperature drops to −50 °C, $\dot{Q}_{leak}$ decreases to about 1.9 kW. By substituting $\dot{Q}_{leak}$ into the above equations, the liquid fuel volume fraction $y_l(t)$ in the tank and the vapor venting mass flow rate $\dot{m}_v$ can be solved. The obtained $\dot{m}_v$ as a function of time during the flight is shown in Fig. 7(b). During the transition from the climb phase to cruising, and throughout the cruising phase, the vapor venting mass flow rate $\dot{m}_v$ constitutes only a few percent of the fuel mass flow rate $\dot{m}_{req}$ supplied to the power system components. To minimize fuel losses, the vented vapor can be redirected to downstream fuel cell stacks, ensuring that no hydrogen is wasted while maintaining optimal system performance.

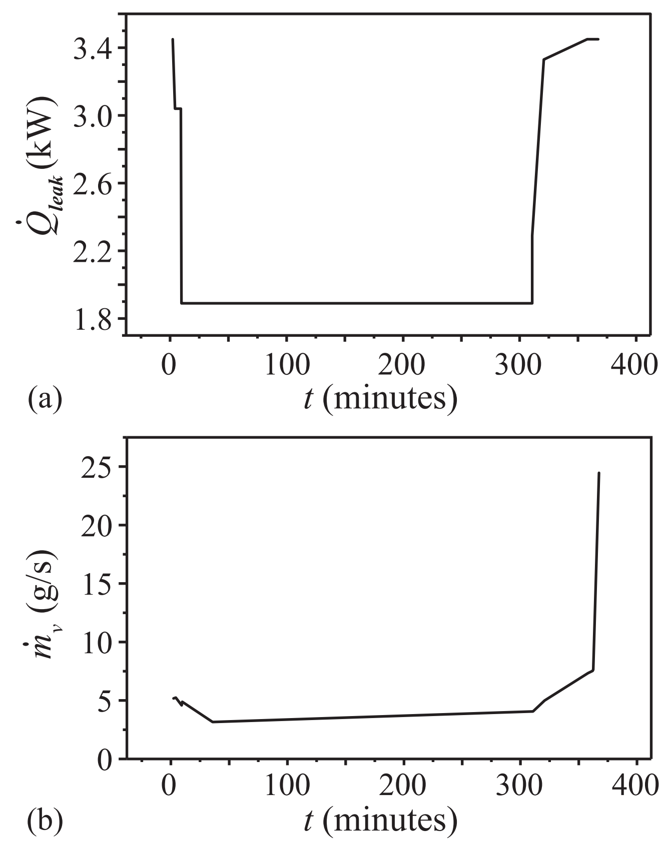

Fig. 7. (a) Calculated heat leakage rate $\dot{Q}_{leak}$ through the hydrogen tank wall for the optimal design configuration; (b) derived vapor venting mass flow rate $\dot{m}_v$ for maintaining the desired tank pressure profile during the flight.

4. Summary

We have presented a comprehensive framework for the design and optimization of an LH_2 storage, thermal management, and transfer-control system to support the IZEA mission. The study demonstrates the successful regulation of tank pressure and hydrogen mass flow rates to meet varying flight power demands while effectively managing the thermal loads of power system components. Key findings emphasize the importance of system-level optimization, balancing storage, transfer, and cooling efficiency to maximize the overall gravimetric index—a critical measure of fuel storage efficiency. The integration of counterflow heat exchangers into the system illustrates the feasibility of using LH_2 as both a fuel and a cooling medium, showcasing its dual functionality in addressing both energy and thermal management needs. This work underscores the potential of LH_2-based systems in advancing sustainable and efficient aviation technologies.

In the future, we plan to address two critical challenges for advancing the IZEA mission. First, the design of heat exchangers within each circulation loop, tasked with transferring heat from the power system components to the working fluid, will be a key focus. Although the current study analyzes the heat exchanger responsible for transferring heat from the working fluid to the fuel pipeline, the absence of detailed specifications for the size, material, and thermal properties of the power system components has prevented the inclusion of these additional heat exchangers. Future efforts will resolve these gaps, enabling their design and incorporation into system-level optimization to achieve an ideal balance of thermal performance, weight, and efficiency. Second, innovative thermal management strategies for cooling the fuel cell stacks will be developed to address the significant heat generation during operation. One promising solution involves conducting heat to the aircraft's body and utilizing skin cooling with cold ambient air at high altitudes, offering an efficient and lightweight means of dissipating heat. These advancements are crucial for refining the overall thermal management architecture and ensuring the practical implementation of zero-emission aviation technologies.

CRediT authorship contribution statement

Parmit S. Virdi: Writing – review & editing, Writing – original draft, Methodology, Formal analysis. **Wei Guo:** Writing – review & editing, Writing – original draft, Supervision, Resources, Project administration, Methodology, Funding acquisition, Formal analysis, Conceptualization. **Peter Cheetham:** Writing – review & editing, Funding acquisition. **Lance Cooley:** Writing – review & editing, Funding acquisition. **Jonathan C. Gladin:** Writing – review & editing, Funding acquisition. **Jiangbiao He:** Writing – review & editing, Funding acquisition. **Chul Kim:** Writing – review & editing, Funding acquisition. **Hui Li:** Writing – review & editing, Funding acquisition. **Juan Ordonez:** Writing – review & editing, Funding acquisition. **Sastry Pamidi:** Writing – review & editing, Funding acquisition. **Jian-Ping Zheng:** Writing – review & editing, Funding acquisition.

Declaration of competing interest

The authors declare that they have no known competing financial interests or personal relationships that could have appeared to influence the work reported in this paper.

Acknowledgments

The authors acknowledge the support from NASA under award 80NSSC22M0068. The work was conducted at the National High Magnetic Field Laboratory at Florida State University, which is supported by the National Science Foundation Cooperative Agreement No. DMR-2128556 and the State of Florida.

Data availability

Data will be made available on request.

References

[1] Baroutaji A, Wilberforce T, Ramadan M, Olabi AG. Comprehensive investigation on hydrogen and fuel cell technology in the aviation and aerospace sectors. Renew Sustain Energy Rev 2019;106:31–40. https://doi.org/10.1016/j.rser.2019.02.022.
[2] Yusaf T, Fernandes L, Abu Talib AR, Altarazi YS, Alrefae W, Kadirgama K, et al. Sustainable aviation—hydrogen is the future. Sustainability 2022;14(1):548. https://doi.org/10.3390/su14010548.
[3] Terrenoire E, Hauglustaine DA, Gasser T, Penanhoat O. The contribution of carbon dioxide emissions from the aviation sector to future climate change. Environ Res Lett 2019;14(8):084019. https://doi.org/10.1088/1748-9326/ab3086.
[4] Larsson J, Elofsson A, Sterner T, Åkerman J. International and national climate policies for aviation: a review. Clim Policy 2019;19(6):787–99. https://doi.org/10.1080/14693062.2018.1562871.
[5] Choi Y, Lee J. Estimation of liquid hydrogen fuels in aviation. Aerospace 2022;9(10):564. https://doi.org/10.3390/aerospace9100564.
[6] Winnefeld C, Kadyk T, Bensmann B, Krewer U, Hanke-Rauschenbach R. Modelling and designing cryogenic hydrogen tanks for future aircraft applications. Energies 2018;11(1):105. https://doi.org/10.3390/en11010105.
[7] Mital SK, Gyekenyesi JZ, Arnold SM, Sullivan RM, Manderscheid JM, Murthy PL. Review of current state of the art and key design issues with potential solutions for liquid hydrogen cryogenic storage tank structures for aircraft applications. NASA report NASA/TM—2006-214346; 2006.
[8] Qiu Y, Yang H, Tong L, Wang L. Research progress of cryogenic materials for storage and transportation of liquid hydrogen. Metals 2021;11(7):1101. https://doi.org/10.3390/met11071101.
[9] Jakupca I. Electrified aircraft propulsion integration concepts: primary fuel cells and cryogenic hydrogen storage. NASA technical reports server; 2023. https://ntrs.nasa.gov/citations/20230012889.
[10] Massaro MC, Biga R, Kolisnichenko A, Marocco P, Monteverde AHA, Santarelli M. Potential and technical challenges of on-board hydrogen storage technologies coupled with fuel cell systems for aircraft electrification. J Power Sources 2023;555:232397. https://doi.org/10.1016/j.jpowsour.2022.232397.
[11] Podlaski M, Khare A, Vanfretti L, Sumption M, Ansell P. Multi-domain modeling for high temperature superconducting components for the CHEETA hybrid propulsion power system. In: 2021 AIAA/IEEE electric aircraft technologies symposium (EATS); IEEE; 2021. p. 1–10. https://doi.org/10.23919/EATS52162.2021.9704847.
[12] Stautner W, Ansell PJ, Haran KS. CHEETA: an all-electric aircraft takes cryogenics and superconductivity on board: combatting climate change. IEEE Electrif Mag 2022;10(2):34–42. https://doi.org/10.1109/MELE.2022.3165948.
[13] Tiwari S, Pekris MJ, Doherty JJ. A review of liquid hydrogen aircraft and propulsion technologies. Int J Hydrogen Energy 2024;57:1174–96. https://doi.org/10.1016/j.ijhydene.2023.12.263.
[14] Gladin JC, Paatel S, Ahuja J, Mavris D. Near zero emissions Flight enabled by a robust hybrid-electric architecture. In: AIAA aviation forum and ASCEND; 2024. p. 3630. https://doi.org/10.2514/6.2024-3630.
[15] Khan MAH, Brierley J, Tait KN, Bullock S, Shallcross DE, Lowenberg MH. The emissions of water vapour and NO_x from modelled hydrogen-fuelled aircraft and the impact of NO_x reduction on climate compared with kerosene-fuelled aircraft. Atmosphere 2022;13(10):1660. https://doi.org/10.3390/atmos13101660.
[16] Mourouzidis C, Singh G, Sun X, Huete J, Nalianda D, Nikolaidis T, et al. Abating CO_2 and non-CO_2 emissions with hydrogen propulsion. Aeronaut J 2024;128(1325):1–18. https://doi.org/10.1017/aer.2024.20.
[17] Sehra AK, Whitlow W Jr. Propulsion and power for 21st century aviation. Prog Aerosp Sci 2004;40(4–5):199–235. https://doi.org/10.1016/j.paerosci.2004.06.003.
[18] Lei T, Min Z, Gao Q, Song L, Zhang X, Zhang X. The architecture optimization and energy management technology of aircraft power systems: a review and future trends. Energies 2022;15(11):4109. https://doi.org/10.3390/en15114109.
[19] Srinath AN, Pena López Á, Miran Fashandi SA, Lechat S, di Legge G, Nabavi SA, et al. Thermal management system architecture for hydrogen-powered propulsion technologies: practices, thematic clusters, system architectures, future challenges, and opportunities. Energies 2022;15(1):304. https://doi.org/10.3390/en15010304.
[20] Sparano M, Sorrentino M, Troiano G, Cerino G, Piscopo G, Basaglia M, et al. The future technological potential of hydrogen fuel cell systems for aviation and preliminary co-design of a hybrid regional aircraft powertrain through a mathematical tool. Energy Convers Manag 2023;281:116822. https://doi.org/10.1016/j.enconman.2023.116822.
[21] Ansell PJ. Hydrogen-electric aircraft technologies and integration: enabling an environmentally sustainable aviation future. IEEE Electrif Mag 2022;10(2):6–16. https://doi.org/10.1109/MELE.2022.3165721.
[22] Climente-Alarcon V, Baskys A, Patel A, Glowacki BA. Analysis of an on-line superconducting cryofan motor for indirect cooling by LH_2. IOP Conf Ser Mater Sci Eng 2019;502(1):012050. https://doi.org/10.1088/1757-899X/502/1/012050.
[23] Barbir F, Balasubramanian B, Neutzler J. Optimal operating temperature and pressure of PEM fuel cell systems in automotive applications. In: Abstracts of papers of the American Chemical Society, vol. 218; 1999. p. U637.
[24] Mueller E, Chatterji G. Analysis of aircraft arrival and departure delay characteristics. In: AIAA's aircraft technology, integration, and operations (ATIO) 2002 technical forum; 2002. p. 5866. https://doi.org/10.2514/6.2002-5866.
[25] Gomez A, Smith H. Liquid hydrogen fuel tanks for commercial aviation: structural sizing and stress analysis. Aerosp Sci Technol 2019;95:105438.
[26] Dampfkesselausschuss D, Essen T. Technische Regeln für dampfkessel. Berlin, Germany: Verband der TÜV eV; 2010.
[27] Kameni Monkam L, Graf von Schweinitz A, Friedrichs J, Gao X. Feasibility analysis of a new thermal insulation concept of cryogenic fuel tanks for hydrogen fuel cell powered commercial aircraft. Int J Hydrogen Energy 2022;47(73):31395–408. https://doi.org/10.1016/j.ijhydene.2022.07.069.
[28] Burschyk T, Cabac Y, Silberhorn D, Boden B, Nagel B. Liquid hydrogen storage design trades for a short-range aircraft concept. CEAS Aeronaut J 2023;14(4):879–93. https://doi.org/10.1007/s13272-023-00689-4.
[29] Huete J, Pilidis P. Parametric study on tank integration for hydrogen civil aviation propulsion. Int J Hydrogen Energy 2021;46(74):37049–62. https://doi.org/10.1016/j.ijhydene.2021.08.194.
[30] Silberhorn D, Atanasov G, Walther J-N, Zill T. Assessment of hydrogen fuel tank integration at aircraft level. In: Deutscher Luft-und Raumfahrtkongress; 2019.
[31] Sharifzadeh S, Verstraete D, Hendrick P. Cryogenic hydrogen fuel tanks for large hypersonic cruise vehicles. Int J Hydrogen Energy 2015;40(37):12798–810. https://doi.org/10.1016/j.ijhydene.2015.07.120.
[32] Sharke P. H_2 tank testing. Mech Eng-C 2004;126(4):20–1.
[33] Timmerhaus KD, Reed RP. Cryogenic engineering: fifty years of progress. New York: Springer Science & Business Media; 2007.
[34] Mann D. LNG materials and fluids: a user's manual of property data in graphic format. Boulder, CO: National Bureau of Standards; 1977. https://www.osti.gov/biblio/6271374.
[35] Bejan A. Convection heat transfer. Hoboken, (NJ): John Wiley & Sons; 2013.
[36] Masson PJ, Brown GV, Soban DS, Luongo CA. HTS machines as enabling technology for all-electric airborne vehicles. Supercond Sci Technol 2007;20(8):748. https://doi.org/10.1088/0953-2048/20/8/005.
[37] Jin JX, Tang YJ, Xiao XY, Du BX, Wang QL, Wang JH, et al. HTS power devices and systems: principles, characteristics, performance, and efficiency. IEEE Trans Appl Supercond 2016;26(7):1–26. https://doi.org/10.1109/TASC.2016.2602346.

[38] Berg F, Palmer J, Miller P, Dodds G. HTS system and component targets for a distributed aircraft propulsion system. IEEE Trans Appl Supercond 2017;27(4):1–7. https://doi.org/10.1109/TASC.2017.2652319.

[39] Ordonez J, Sailabada C, Guo W, Cooley L, Cheetham P, Kim C, et al. Thermal management challenges and approaches for liquid hydrogen-fueled aircraft. In: AIAA aviation forum and ASCEND; 2024. p. 3877. https://doi.org/10.2514/6.2024-3877.

[40] Pamidi S, Kim C, Graber L. High-temperature superconducting (HTS) power cables cooled by helium gas. In: Superconductors in the power grid. Elsevier; 2015. p. 225–60. https://doi.org/10.1016/B978-1-78242-029-3.00007-8.

[41] Hartwig ZS, Vieira RF, Dunn D, Golfinopoulos T, LaBombard B, Lammi CJ, et al. The SPARC toroidal field model coil program. IEEE Trans Appl Supercond 2023. https://doi.org/10.1109/TASC.2023.3332613.

[42] Barber JJV. Investigation of cryogenic cooling for a high-field toroidal field magnet used in the sparc fusion reactor design [Ph.D. thesis]. Massachusetts Institute of Technology; 2018.

[43] Schaefer S, Quaium F, Muhsal N, Speerforck A, Thielecke F, Becker C. Integration of a cooling system architecture with a skin heat exchanger for high thermal loads in fuel cell powered aircraft; 2022.

[44] Shah R, Sekulic D. Handbook of heat transfer, vol. 3. New York; McGraw–Hill; 1998.

[45] National Institute of Standards and Technology (NIST). Thermophysical properties of fluid systems. NIST chemistry WebBook. NIST standard reference database number 69; 2024. https://webbook.nist.gov/chemistry/fluid/.

[46] Yunus A, John M, Afshin J. Thermal fluid sciences. 5th ed. Asia: McGraw Hill; 2016.

[47] Vassallo P, Keller K. Two-phase frictional pressure drop multipliers for SUVA R-134a flowing in a rectangular duct. Int J Multiphase Flow 2006;32(4):466–82. https://doi.org/10.1016/j.ijmultiphaseflow.2006.01.004.

[48] Kundu PK, Cohen IM, Dowling DR, Capecelatro J. Fluid mechanics. 6th ed. San Diego: Elsevier; 2024.

[49] Cryogenic Fans; 2024. https://stirlingcryogenics.com. [Accessed February 21].

[50] ASME. Process piping: ASME code for pressure piping B31. New York: American Society of Mechanical Engineers Press; 2016.

[51] Alrsai M, Karampour H, Albermani F. On collapse of the inner pipe of a pipe-in-pipe system under external pressure. Eng Struct 2018;172:614–28. https://doi.org/10.1016/j.engstruct.2018.06.057.

[52] Magnatex Pumps; 2024. https://magnatexpumps.com/mep.php [Accessed June 10].